

The plane-parallel albedo bias of liquid clouds from MODIS observations

Lazaros Oreopoulos^{1,2}, Robert F. Cahalan^{2,1}, and Steven Platnick^{2,1}

1. Joint Center for Earth Systems Technology, University of Maryland Baltimore County, Baltimore, MD

2. Laboratory for Atmospheres, NASA Goddard Space Flight Center, Greenbelt, MD

Revised for the J. Climate

March 2007

Corresponding author address:

Lazaros Oreopoulos
NASA-GSFC
Code 613.2
Greenbelt, MD 20771

Abstract

We present the global plane-parallel shortwave albedo bias of liquid clouds for two months, July 2003 and January 2004. The cloud optical properties necessary to perform the bias calculations come from the operational MODIS Terra and MODIS Aqua Level-3 datasets. These data, along with ancillary surface albedo and atmospheric information consistent with the MODIS retrievals, are inserted into a broadband shortwave radiative transfer model to calculate the fluxes at the atmospheric column boundaries. The Plane-Parallel Homogeneous (PPH) calculations are based on the mean cloud properties, while Independent Column Approximation (ICA) calculations are based either on 1D histograms of optical thickness or joint 2D histograms of optical thickness and effective radius. The (positive) PPH albedo bias is simply the difference between PPH and ICA albedo calculations. Two types of biases are therefore examined: (1) the bias due to the horizontal inhomogeneity of optical thickness alone (the effective radius is set to the grid mean value); and (2) the bias due to simultaneous variations of optical thickness and effective radius as derived from their joint histograms. We find that the global bias of albedo (liquid cloud portion of the gridboxes only) is $\sim +0.03$ which corresponds to roughly 8% of the global liquid cloud albedo, and is only modestly sensitive to the inclusion of horizontal effective radius variability and time of day, but depends strongly on season and latitude. This albedo bias translates to $\sim 3\text{--}3.5 \text{ Wm}^{-2}$ of bias (stronger negative values) in the diurnally-averaged global shortwave cloud radiative forcing, assuming homogeneous conditions for the fraction of the gridbox not covered by liquid clouds; zonal values can be as high as 8 Wm^{-2} . Finally, the (positive) broadband atmospheric absorptance bias is about an order of magnitude smaller than the albedo bias. The substantial magnitude of the PPH bias underlines the importance of predicting subgrid variability in GCMs and accounting for its effects in cloud-radiation interactions.

1. Introduction

The bias in solar radiative fluxes within a model or other large-scale grid due to the assumption of horizontal homogeneity in cloud optical thickness τ (Plane-Parallel Homogeneous–PPH– bias) received a great amount of attention following the publication of the study by Cahalan et al. (1994), but its existence and potential importance had already emerged in earlier publications (Harshvardhan and Randall, 1985; Stephens 1988). Cahalan et al. provided a theoretical framework for studying the PPH bias by using a fractal cloud model, but restricted the quantitative analysis of cloud inhomogeneity on marine stratocumulus clouds with properties derived from surface microwave radiometer observations. Cloud microphysics (i.e., droplet effective radius, r_e) was assumed constant ($r_e=10\text{ }\mu\text{m}$), surface and atmospheric effects were neglected, and the radiative transfer did not extend beyond monochromatic calculations. For typical marine stratocumulus observed during the First ISCCP (International Satellite Cloud Climatology Project) Regional Experiment (FIRE), Cahalan et al. found a value of $\sim+0.09$ as representative of the PPH albedo bias at visible wavelengths. Subsequent observationally-based work (Barker 1996, Oreopoulos and Davies 1998; Pincus et al., 1999; Rossow et al. 2002) provided additional estimates of average PPH albedo bias that ranged from $+0.02$ to $+0.3$ depending on spectral range, cloud type, spatial resolution of the satellite observations, and reference area size. Bias estimates of reflected solar flux (or equivalently shortwave cloud radiative forcing) were also derived for cloud fields provided by the Multiscale Modeling Framework (Khairoutdinov et al., 2005) by Räisänen et al., (2004) and Oreopoulos et al. (2004), but these were limited to a very

short (24 hours) time period, and included compensating errors due to the specific cloud fraction overlap assumptions in the radiative transfer codes.

The present study provides the most extensive hitherto estimates of PPH bias for liquid clouds. Specifically, we present global distributions of broadband albedo and cloud radiative forcing bias based on two entire months of MODIS liquid water cloud retrievals that also account for the effects of atmospheric absorption and surface reflectance by using the same ancillary data sets used in the retrievals. Since the calculations are broadband and refer to the entire atmospheric column, estimates of the bias in solar radiation absorbed by the atmosphere is examined as well. We also take advantage of the availability of joint optical τ - r_e histograms to compare the biases due to the combined τ - r_e variability with those solely due to variability in τ .

The dataset and computational details are explained in the next section; results are presented in the five subsections of section 3, and conclusions, as well as suggestions on how to use the results for model validation, are provided in section 4.

2. Dataset and radiative transfer calculations

We use daily MODIS Level-3 (1° resolution gridded) data from both the Terra (~ 1030 local time overpass) and Aqua (~ 1330 overpass) satellites (datasets MOD08_D3 and MYD08_D3, respectively). This high-level dataset, obtained from the Collection 4 processing stream, contains the mean daily values of vertically integrated optical thickness ($\bar{\tau}$), effective radius (\bar{r}_e), cloud fraction of successful cloud retrievals, and solar zenith angle (SZA), as well as one-dimensional (1D) and joint (2D) histograms of τ and r_e (King et al., 2003) constructed by sampling every 5th retrieval at the original 1 km

resolution. For liquid clouds used in this study, the 1D histograms of τ are resolved in 45 bins; the 2D histograms of τ and r_e are resolved in 110 bins (11 for τ and 10 for r_e). Except for high latitudes where gridboxes can be revisited within the same day due to orbital swath overlap, the daily histograms mainly represent the instantaneous spatial variability of τ and r_e within the $1^\circ \times 1^\circ$ gridbox.

The radiative transfer calculations yielding daily atmospheric column albedo, transmittance, and absorptance are performed with a modified version of the broadband (BB) shortwave (SW) Column Radiation Model (CORAM) described by Chou et al. (1998). The model can provide the flux profile of the entire atmospheric column, either over the entire solar spectrum (0.2–5.0 μm), or over the ultraviolet-visible (UV-VIS, 0.2–0.7 μm) and near-infrared (NIR, 0.7–5.0 μm) bands separately. It can account for molecular, aerosol and cloud absorption and scattering, and surface reflection with and without a vegetation canopy. Since our calculations do not include the portion of the gridbox covered by ice clouds or clear skies, and liquid clouds are assumed to form in single layers, the cloud fraction overlap assumptions of the model are not used. To isolate the albedo and absorptance due the liquid clouds themselves, one can easily switch off the atmosphere and surface contributions (identified in this paper as cloud-only calculations). We compare results of both types of calculations, full-column (FC) and cloud-only (CO) in section 3. For FC calculations, the values of surface albedo and the concentrations of active atmospheric absorbers, H_2O (profile), O_3 (column amount), and CO_2 are required; aerosols are neglected.

Ancillary surface spectral albedo comes from the identical data sources and methods used in the operational MODIS cloud retrievals. The snow-free and permanent snow/ice

albedo is the 5-year climatology of Moody et al. (2005), which uses an ecosystem-dependent temporal interpolation technique to fill missing or seasonally snow-covered data in the operational MODIS Terra surface albedo product (MOD43B3). The data are provided in a 1 arc minute equal-angle grid with the seasonal cycle resolved in 16-day periods. Snow and ice scenes are identified with the snow/ice index from National Oceanic and Atmospheric Administration (NOAA) microwave-derived daily 0.25° Near Real-Time Ice and Snow Extent (NISE) dataset. Spectral albedos for non-permanent snow on land surfaces are taken from lookup tables populated by seasonal MOD43B3 albedos aggregated by the MODIS Terra ecosystem product (MOD12Q1). Sea-ice albedo is derived from a combination of permanent snow/ice and open-ocean albedo along with an estimate for the melt-season transition. In all cases, we use the diffuse (“white-sky”) albedo for the broad 0.3–0.7 μm and 0.7–5.0 μm bands which roughly correspond to the UV-VIS and NIR bands of the Chou et al. (1998) model.

Atmospheric profiles of temperature and water vapor are resolved into 16 layers extending from 1000 to 10 mb and come from the National Center for Environmental Prediction (NCEP) Global Data Assimilation System (GDAS) product (Derber et al., 1991). This data set is identical to the one used in the operational MODIS retrievals. The product also provides total (column) ozone concentration. The CO_2 concentration is set at 370 ppm. The cloud is placed in the layer whose top temperature is closest to the mean cloud top temperature (\bar{T}_c) as derived from the joint histogram of liquid cloud τ and T_c .

A significant modification to our version of the CORAM is the introduction of a new method of calculating cloud optical properties (extinction, single-scattering albedo, asymmetry parameter). It essentially consists of look-up tables of these properties as a

function of r_e for the four (one in the UV-VIS and three in the NIR) broad spectral intervals of the model. These look-up tables are based on the tabulated values of Hu and Stamnes (1993) and allow calculation of optical properties for $r_e > 20 \mu\text{m}$ which was not possible with the original Chou et al. (1998) parameterization. The visible values of τ from the MODIS dataset correspond to UV-VIS band of the CORAM, and the spectral values of τ for the remaining three bands in the NIR are found by rescaling the visible τ with the ratio of the extinction coefficient of the NIR band corresponding to the retrieved r_e to its counterpart in the UV-VIS band.

Three different albedos (R) are calculated with CORAM: (1) albedos using the $\bar{\tau}$ and \bar{r}_e values of the gridbox (the PPH albedo R_{PPH}); (2) albedos using the 1D histogram of τ and the gridbox mean value of effective radius \bar{r}_e (type 1 ICA albedo R_{ICA1}), i.e., obtained from multiple albedo calculations weighted by the relative frequency in each τ bin; and (3) albedos using the 2D histogram (type 2 ICA albedo R_{ICA2}), i.e., obtained from multiple albedo calculations weighted by the relative frequency in each (τ, r_e) bin. The albedo calculated with the first method minus that calculated with the second gives the classic plane-parallel albedo bias with constant microphysics ($B_1^R > 0$). The albedo calculated with the first method minus that calculated with the third gives the albedo bias due to horizontal variations of both τ and r_e ($B_2^R > 0$). Mathematically, the biases can be expressed as follows:

$$B_1^R(\bar{\tau}, \bar{r}_e, \nu_\tau, \mu_0) = R_{PPH} - R_{ICA1} \equiv \mathbf{R}(\bar{\tau}, \bar{r}_e, \mu_0) - \int \mathbf{R}(\tau, \bar{r}_e, \mu_0) p(\tau) d\tau \quad (1a)$$

$$B_2^R(\bar{\tau}, \bar{r}_e, \nu_{\tau, r_e}, \mu_0) = R_{PPH} - R_{ICA2} \equiv \mathbf{R}(\bar{\tau}, \bar{r}_e, \mu_0) - \iint \mathbf{R}(\tau, r_e, \mu_0) p(\tau, r_e) d\tau dr_e \quad (1b)$$

where μ_0 is the cosine of the solar zenith angle, ν is a measure of either τ or joint τ - r_e variability (e.g., a shape parameter of the 1-D probability density function $p(\tau)$ or the 2-D probability density function $p(\tau, r_e)$), and \mathbf{R} is the reflectance function (e.g., the analytical solution of the two-stream approximation). The dependencies of the albedo bias on molecular absorption, Rayleigh scattering, and surface albedo are not explicitly shown in the above equations, so Eqs. (1a) and (1b) are strictly accurate for isolated clouds only. It is understood, however, that all these factors (assumed to be homogeneous within the 1° gridbox) are accounted for in all our FC calculations. Note that our ICA calculations are subject to errors due to the discretization of the 1D and 2D histograms, but these errors are of random nature. Since ICA is based on 1D radiative transfer calculations, it also suffers, of course, from errors arising from neglect of horizontal photon transfer taking place in the real world. These errors of ICA relative to 3D have been documented in numerous occasions in the literature (see Scheirer and Macke, 2003 for a characteristic example of such a study), but will not concern us here since it is unlikely that global models will be able to perform 3D radiative transfer calculations in the near future.

The albedo bias calculations are performed for every day of the month in each gridbox and are then averaged to monthly values using the gridbox cloud fraction of successful liquid water retrievals as a weight. Due to the generally larger uncertainties in the retrievals and parameterization of wide-band optical properties of ice clouds, we restrict the current analysis to liquid water clouds only. We plan to revisit the issue of the ice cloud albedo bias in the future, following derivation of wide-band optical properties for the CORAM that are consistent with the ice crystal size distributions used in the MODIS retrievals.

3. Results

We have performed a large number of bias calculations covering the entire portion of the globe, for which illumination conditions allow MODIS cloud property retrievals, in the manner described previously. The bias calculations were performed for both full (atmosphere-surface) columns containing clouds, and isolated clouds only, for both joint τ - r_e and τ -only variability, for both MODIS Terra and MODIS Aqua, and for both July 2003 and January 2004. Most the results shown below are for full column (FC) calculations, unless explicitly stated otherwise.

a. Terra vs. Aqua and seasonal differences

Figure 1 shows global (area-weighted) monthly-averaged PPH albedo, and PPH albedo biases (B_1^R and B_2^R) from MODIS Terra and MODIS Aqua Level-3 (from FC calculations for the portion of gridboxes covered by liquid clouds and at the mean SZA reported in the MOD08_D3 and MYD08_D3 datasets). For now, we focus on the B_1^R bias only (B_2^R biases are discussed in subsection 3e). The global PPH albedo bias due to variability of liquid cloud vertically integrated optical thickness variations is $\sim +0.03$ and differs only slightly between the two months and between morning (Terra) and afternoon (Aqua). The biases are about 8% of the global PPH albedo (white bars). Interestingly, the bias tends to be larger when the albedo is smaller, i.e., MODIS Aqua for July exhibits the largest relative bias (+8.6%) while MODIS Terra for January the smallest (+7.6%). The small July vs. January differences in global-mean PPH albedo probably reflect (partly compensating) differences in the horizontal distribution of liquid cloud properties, SZA,

surface albedo and errors in the retrievals of cloud properties. The slightly larger overall Aqua bias is consistent with the higher afternoon cloud inhomogeneity found for the same months by Oreopoulos and Cahalan (2005).

Figure 2, plotting the normalized frequency of occurrence distributions of monthly-averaged B_1^R bias for Terra and Aqua, reveals that significant differences lurk behind the apparent similarity between seasonal global values. These distributions were constructed by binning all available monthly-averaged gridbox biases for the two months. The seasonal differences are primarily due to differences in illumination geometry and cloud inhomogeneity. The January histogram has a well-defined peak at an albedo bias of $\sim +0.024$, while for July the frequency of occurrence around these values is smaller by about 30%, and a bimodal behavior can be seen. PPH albedo biases in the range between $+0.03$ and $+0.06$, on the other hand, are observed for a far larger fraction of gridboxes in July. The first peak in the January distribution is attributed to Antarctica gridboxes where the high surface albedos cause dramatic reductions in the PPH bias (distributions of biases calculated assuming black surface are devoid of this peak). Intraday differences are more subtle: the January morning and afternoon distributions are more similar than those for July. This probably reflects the greater diurnal variability of continental clouds compared to marine clouds during the summer: the land-dominated northern hemisphere (NH) exhibits a greater cloud variability in the summer compared to the ocean-dominated southern hemisphere (SH).

b. Geographical distribution

Figure 3 shows the geographical distribution of monthly mean B_1^R bias (from the daily B_1^R biases weighted by liquid cloud fraction) for Terra (the Aqua maps are qualitatively similar). The top and bottom panels are for July 2003 and January 2004, respectively. Again, the bias corresponds only to the portion of the Level-3 $1^\circ \times 1^\circ$ gridboxes occupied by liquid clouds. Atmospheric and surface effects are included in the manner described in the previous section (FC calculations). A distinct contrast between the winter and summer hemispheres is evident. The albedo bias assumes large values in the winter hemisphere oceans, small values in the summer hemisphere oceans, and larger values over land in the NH summer compared to NH winter. The oceanic contrast between winter and summer could perhaps be somehow related to 3D radiative transfer in the real world vs. 1D radiative transfer in the MODIS retrieval algorithm. However, a closer look suggests a link to cloud types: large albedo biases for the often vertically extensive frontal cloud systems in the oceanic storm tracks, and small biases for maritime low clouds in the summer. The biases for the latter ($\sim +0.03$) are more consistent with the satellite-based study of Pincus et al. (1999) than Cahalan et al. (1994) who used surface based retrievals of liquid water path (LWP) and aggregated over temporal scales that correspond to spatial scales larger than those that constitute our reference here.

A comparison of FC and CO albedo bias maps (not shown) reveals that a significant reduction of albedo bias in NH winter land masses occurs because of the increase in (often snow-covered) surface albedo. This effect is especially prominent at Antarctica where the surface albedo is such a large contributor to the FC albedo that the albedo bias is all but eliminated.

Land-ocean contrasts and their seasonal changes are summarized in Figure 4. Hemispherically-averaged B_1^R values obtained by averaging Terra and Aqua biases (solid black and gray bars) are plotted separately for only NH oceanic and continental gridboxes, where their populations are more similar. When examined on this hemispheric basis, the July and January biases are similar only over land. The oceanic biases increase in January compared to July (and become larger than their counterparts over land), most likely due to the substantial increase in the inhomogeneity of marine clouds, while the change much smaller change in continental cloud inhomogeneity (Oreopoulos and Cahalan, 2005) is reflected in the corresponding albedo biases which remain almost unchanged.

c. Bias in cloud radiative forcing

It would be illuminating to convert the global PPH albedo bias of liquid clouds to the bias in the reflected solar flux at TOA ($\Delta F^{all-sky}$) for the entire gridbox (i.e., including the portions of the gridbox covered by ice phase clouds or not covered by clouds at all, assuming homogeneity for both of these cases) in order to compare its magnitude to that of various climate forcings. Assuming no ice clouds in the gridbox (with no loss of generality if the ice clouds are homogeneous) we can show that this reflected flux bias is essentially the absolute value of the bias $\Delta SWCRF^{TOA}$ in (negative) SW liquid Cloud Radiative Forcing $SWCRF$ at TOA. This is because this forcing is nominally defined as

$$SWCRF^{TOA} \equiv F^{clr} - F^{all-sky} = A_c (F^{clr} - F^{cld}) = A_c \mu_0 S_0 (R^{clr} - R^{cld}) \quad (2),$$

and the flux reflected from the cloudless sky portion of the gridbox has no bias. To derive the above we have assumed that the all-sky flux ($F^{all-sky}$) can be expressed as the liquid cloud fraction (A_c)–weighted average of the clear and (liquid) cloudy sky fluxes (F^{clr} and F^{cld} , respectively):

$$F^{all-sky} = (1 - A_c)F^{clr} + A_cF^{cld}.$$

Therefore,

$$\begin{aligned} \Delta SWCRF^{TOA} (< 0) &\equiv SWCRF_{PPH}^{TOA} - SWCRF_{ICA}^{TOA} = \\ &-A_c(F_{PPH}^{cld} - F_{ICA}^{cld}) = -A_c\Delta F^{cld} = -\Delta F^{all-sky} = -A_cB^R\mu_0S_0 \end{aligned} \quad (3),$$

where $\Delta F^{cld} \equiv F_{PPH}^{cld} - F_{ICA}^{cld} > 0$ is the bias in reflected solar flux for the cloudy portion of the gridbox and S_0 is the vertically incident solar flux at TOA.

Absolute values of $\Delta SWCRF^{TOA}$ solely due to optical thickness variations from a variety of FC calculation methods that combine Terra and Aqua biases are shown in Figure 5. Each of the five July and January bars of Fig. 5 corresponds to one of the following types of $SWCRF$ bias calculations: (1) calculations combining the average Terra and Aqua PPH albedo bias described above with the insolation corresponding to the gridbox mean SZA of the MOD08_D3 and MYD08_D3 files (“overpass”) (2) calculations combining the average Terra and Aqua PPH albedo bias described above with the daytime-averaged insolation for the gridbox (“daytime 1”); (3) calculations combining the previously-described average Terra and Aqua PPH albedo bias with the diurnal (24-hour)-averaged insolation for the gridbox (“diurnal 1”); (4) calculations of the daytime average cloud radiative forcing bias obtained by pairing the instantaneous PPH

albedo bias with the instantaneous insolation at 2-hour intervals, whenever the sun is above the horizon (“daytime 2”); (5) calculations scaling the latter values to 24-hour periods (“diurnal 2”). In the last two types of calculations clouds are assumed unchanged during the 12-hour period that precedes (for Terra calculations) and follows (for Aqua calculations) local solar noon. Type (4) calculations are significantly more intensive computationally than the original PPH albedo bias calculations since they involve multiple bias calculations per day for each gridbox. Somewhat surprisingly, however, type (2) and type (4) and, consequently, type (3) and type (5) calculations give almost the same value of global (absolute) *SWCRF* bias. This implies that the albedo bias calculated at the gridbox-mean SZA (closely linked to SZAs at overpass times) can be used as a representative of the albedo bias for the entire day for *SWCRF* bias calculations, under the assumption that clouds remain unchanged during each of the 12- hour periods centered around local noon.

As expected, type (1) *SWCRF* biases, corresponding to the higher SZA values close to local noon, provide the highest values ($\sim 8.5\text{--}9 \text{ Wm}^{-2}$). Daytime and diurnal *SWCRF* biases are about 25% ($\sim 6\text{--}6.5 \text{ Wm}^{-2}$) and 60% ($3\text{--}3.5 \text{ Wm}^{-2}$) smaller. The higher January *SWCRF* biases are partly due to the shorter Earth-Sun distance for this month. It is apparent that the PPH *SWCRF* bias of liquid clouds is a substantial fraction of the global *SWCRF* due to all types of clouds (approximately -50 Wm^{-2} according to Kiehl and Trenberth 1997) and is larger than most of the climate forcings studied in the context of climate change.

d. Relationship between PPH bias and cloud inhomogeneity

The geographical distribution of albedo bias in Fig. 3 correlates with the geographical distribution of the inhomogeneity parameter χ (ratio of logarithmic to linear τ mean) shown in Fig. 7 of Oreopoulos and Cahalan (2005): large values of albedo bias generally correspond to small values of χ (large cloud inhomogeneity) and vice-versa. Figure 6 collects the PPH biases and χ values of these two plots for July 2003 and displays them in the form of a scatterplot (i.e., each point represents a MODIS Terra July 2003 $1^\circ \times 1^\circ$ gridbox where it was possible to make liquid cloud χ and bias estimates). While the expected anticorrelation is present, there is also considerable scatter, not only because of the averaging at monthly scales, but also because of the influence of a host of other factors besides inhomogeneity (values of mean optical thickness, SZA, and surface albedo, strength of atmospheric absorption and scattering) on the albedo bias values. For example, gridboxes in the NH near-equatorial and subtropical central Pacific assume small albedo bias values ($\sim +0.005$ – $+0.02$) despite χ values in the range of 0.6–0.7. This is because of the small values of $\bar{\tau}$ (~ 5), making the dependence of albedo on optical thickness quasi-linear. The surface albedo in this case of marine clouds has a minimal effect on the PPH bias. Even if the bias is expressed in units of cloud radiative forcing (see Eq. (3) above) the magnitude of the bias would remain small despite the relatively high insolation. This is because the fractions of liquid phase clouds are also small in this part of the world, in addition to the small optical thicknesses.

The breakdown of the relationship between cloud inhomogeneity and *SWCRF* bias is actually a more general finding that becomes evident when examining Fig. 7. The top panel of this figure combines the Terra and Aqua zonal curves of χ for liquid clouds

shown in the top panel of Fig. 4 in Oreopoulos and Cahalan (2005). The bottom panel of Fig. 7 plots the zonally-averaged monthly values of combined Terra-Aqua $\Delta SWCRF^{TOA}$ from type (5) (diurnal) FC $SWCRF$ bias calculations. The $SWCRF$ bias varies considerably with latitude and the zonal-averages reach values as high as 8 Wm^{-2} in the mid- and high latitudes of the summer hemispheres when the diurnally-averaged insolation is large. Only one of these maxima, however, (in the NH) corresponds to a local maximum in cloud inhomogeneity (local minimum of χ). Also, note the relatively small values of $\Delta SWCRF^{TOA}$ in the winter mid-latitudes and in the tropics, modulated by low insolation and low cloud fraction values respectively, even though this is where the most inhomogeneous liquid clouds can be found. In other words, cloud inhomogeneity is stronger when it radiatively matters less! The exception to the rule of high insolation driving $\Delta SWCRF^{TOA}$ are the summer polar regions where the albedo biases are small due to the presence of thick clouds and highly reflective surfaces.

e. Bias reduction due to horizontal variability in r_e

When one considers r_e horizontal variability in addition to τ variability, the PPH albedo bias is reduced, but only by a modest amount. Figure 1 shows the global impact of combined τ - r_e variability. With r_e variability also accounted for, albedo biases decrease by ~ 0.001 - 0.003 (~ 2.7 - 7.5%) (the largest value corresponding to MODIS Terra in July and the smallest for MODIS Aqua in January). These small numbers do not necessarily contradict previous studies (Räisänen et al., 2003; Barker and Räisänen, 2004) on the effects of r_e horizontal variations since in those prior studies the other cloud property that was varying horizontally was not τ , as in our case, but rather cloud water (from aircraft

measurements in Räisänen et al., 2003 and from the Multi-Scale Modeling Framework model in Barker and Räisänen, 2004). As a result, the inferred τ variability in those studies was the aggregate of combined r_e and water content variability (in other words, r_e variability was also driving cloud extinction variability). Here the τ variability is given from the simultaneous combined τ - r_e MODIS retrievals, so that r_e variability is only affecting asymmetry factor and single-scattering albedo variability. To put it another way, the (negative) contribution to the PPH bias arising from r_e spatial variability is, in our case, due to the concavity of the albedo vs. r_e curve under constant τ , which is weak (Fig. 8, solid line). In contrast, the concavity of the albedo vs. r_e curve under constant LWP is strong (Fig. 8, dotted line), and maximizes the influence of r_e variations in Räisänen et al., and Barker and Räisänen. Given this interpretation, it is not surprising that the histograms of PPH albedo bias including r_e variability have the same shape as those for only τ variability, but are shifted slightly to the left (Fig. 9), in a manner consistent with a more or less uniform reduction in albedo bias.

In terms of TOA *SWCRF* bias, the global effect of r_e spatial variability is a reduction of the absolute value of the bias by up to 0.8 Wm^{-2} for type 1 (“overpass”) bias and up to 0.6 Wm^{-2} and 0.3 Wm^{-2} for daytime and diurnal biases. While the contribution of r_e spatial variability to *atmospheric SWCRF* bias (see next subsection) is expected to be even smaller for liquid phase clouds on diurnally-averaged global scales, this type of variability has been shown to yield significant increases in the instantaneous absorptance of convective clouds, when full 3D radiative transfer effects are accounted for (Scheirer and Macke, 2003).

f. The impact of including atmospheric/surface effects and the absorptance bias

Some of the previous estimate of PPH albedo bias (Cahalan et al. 1994, Barker 1996, Pincus et al., 1999) were implicitly quasi-monochromatic and applied to visible wavelengths and marine clouds only for which the influence of the underlying dark ocean surface can be neglected. The global nature of the current PPH albedo bias calculations which now cover the entire solar spectrum no longer allows these simplifications. The impact of including surface albedo and atmospheric absorption in the bias calculations can be gauged by simply comparing the bias from FC and CO (i.e., removing the atmosphere and surface) calculations. This is done for the NH by aggregating separately biases for land and ocean gridboxes and averaging the Terra and Aqua results (Fig. 4). The CO biases are significantly higher, reflecting the fact that the contribution of clouds to the TOA albedo and any perturbation to the TOA albedo, such as due to cloud inhomogeneity, is smaller when atmospheric and surface effects are accounted for. As expected, the difference between the biases is more pronounced over the continents (~75% vs. ~50% over the oceans) where the surface albedos are generally higher.

Since we are performing BB calculations, it is meaningful to also examine the PPH bias of the flux absorbed at the surface and in the atmosphere. This can be done either in terms of normalized flux (unitless) or cloud radiative forcing (Wm^{-2}). The PPH bias for transmittance T ($B^T < 0$) can be defined similarly to the PPH bias for reflectance B^R given by Eq. (1). The PPH bias of atmospheric absorptance A , is simply given by:

$$B^A(> 0) = -B^T(1 - a_{sfc}) - B^R \quad (4)$$

since

$$A = 1 - T(1 - a_{sfc}) - R \quad (5)$$

where a_{sfc} is the surface albedo.

B^A is rarely greater than 10% of B^R as shown in Fig. 10 depicting the correlation between monthly-averaged B_1^R and B_1^A for isolated clouds (top) and for clouds embedded in the full surface-atmosphere column system (bottom). Each point in the plot is a gridbox for which bias estimates were possible for MODIS Terra July 2003 data. The correlation is much better for CO (coefficient of linear correlation $r=0.81$) than FC calculations ($r=0.52$). This reflects the fact that total atmospheric absorptance (including clouds) does not correlate in a simple manner with absorptance due to isolated clouds since clouds absorb a fraction of the solar radiation that would have otherwise been available to atmospheric gases to absorb. Also, note that the cloud absorptance bias is larger than the atmospheric absorptance bias. This echoes the results of Fig. 4 showing albedo biases with and without atmospheric and surface effects.

If, similar to TOA (Eq. 2), one defines the shortwave cloud radiative forcing at the surface $SWCRF^{SFC}$ as the difference of the all-sky minus the clear-sky fluxes absorbed at the surface (generally negative), then the (generally positive) shortwave cloud radiative forcing in the atmosphere $SWCRF^{ATM}$ (difference of all-sky minus clear-sky fluxes absorbed in the atmosphere) from Eqs. (2) and (5) is simply the difference of the TOA minus surface cloud radiative forcings, so the corresponding PPH biases are simply related by:

$$\Delta SWCRF^{ATM} = \Delta SWCRF^{TOA} - \Delta SWCRF^{SFC} \quad (6)$$

$\Delta SWCRF^{SFC}$ has a negative sign and assumes larger absolute values than (negative) $\Delta SWCRF^{TOA}$, so that $\Delta SWCRF^{ATM}$ is a positive quantity. We found that global values of $\Delta SWCRF^{ATM}$ due solely to optical thickness variations are $\sim 0.35 \text{ Wm}^{-2}$ for type (5) (diurnally averaged) $SWCRF$ bias which is about 10% of $\Delta SWCRF^{TOA}$ (the same ratio approximately applies when the other methods of $SWCRF$ bias calculation are considered). Thus, while the effects of horizontal cloud inhomogeneity on atmospheric absorption are small, they are nevertheless non-negligible.

4. Discussion and conclusions

We have presented an analysis of the global plane-parallel bias of reflected shortwave radiation due to horizontal inhomogeneity of liquid clouds for two months, July 2003 and January 2004, using MODIS observations and a broadband radiative transfer algorithm. The biases arise from neglect of the subgrid variability of cloud optical thickness and effective radius variations at scales below $\sim 100 \text{ km}$. We found that effective radius horizontal variability has a rather small effect on the albedo bias when the optical thickness variability has already been accounted for. On the other hand, surface and atmospheric effects play a much more important role in determining the biases at the atmospheric column boundaries. Our estimate of the global albedo bias (liquid cloud portion of the gridboxes only) is $\sim +0.03$ which represents an overestimate of $\sim 8\%$ of the global liquid cloud albedo. This albedo bias translates to an overestimate (i.e., a more negative value) of global shortwave cloud radiative forcing by $\sim 3\text{-}3.5 \text{ Wm}^{-2}$ on a 24-hour basis, assuming homogeneous conditions for the portion of the gridbox not covered by liquid clouds; zonal averages of shortwave cloud radiative forcing bias can reach absolute

values as high as 8 Wm^{-2} . These estimates can be compared with the corresponding estimates of Rossow et al. (2002) for a single day (July 15, 1986) using ISCCP cloud retrievals. Their diurnally-averaged global value is 13 Wm^{-2} , which is much larger than ours. It is unclear whether their inclusion of all cloud types and larger reference areas ($\sim 300 \text{ km}$) provide sufficient reasons to account for the difference. But similarly to us, they find that the broadband atmospheric absorptance bias is roughly an order of magnitude smaller than the albedo bias. Maps of albedo bias from ISCCP can be found at <http://isccp.giss.nasa.gov>. While many geographical features for the low cloud category are similar to ours (Fig. 3) there are also differences that may have to do with the different reference area size, the subset of clouds considered, and the contribution of clear-sky albedo in the calculation (this is not clarified at the website).

The substantial global magnitude of the plane-parallel *SWCRF* bias of liquid clouds when one considers that *SWCRF* $\approx -50 \text{ Wm}^{-2}$ globally, due to all types of clouds, stresses the importance of predicting subgrid variability and cloud overlap in GCMs and accounting for their effects in cloud-radiation interactions. The results of this study along with those for cloud inhomogeneity derived from the same MODIS dataset (Oreopoulos and Cahalan, 2005), constitutes a useful radiative validation dataset for GCMs implementing cloud schemes with subgrid prediction capabilities at spatial resolution similar to that of MODIS Level-3 data. We must, however, emphasize that due to the nature and limitations of the MODIS cloud retrievals a number of processing steps would be required before comparing bias estimates from such a GCM with the estimates of this paper: (1) Clouds diagnosed to be of liquid phase at their top and that are unobscured by upper level ice clouds would have to be selected; (2) The PPH bias would have to be

calculated at TOA and only for the cloudy portion of gridboxes with such unobscured clouds (3) Cloud data would have to be sampled only at the local solar times of Terra and Aqua overpasses to simulate type (1) *SWRCF* biases described in subsection 3c. Similar care would have to be exercised, of course, if a MODIS-based ice cloud PPH bias validation dataset emerges in the near future and is used for such a comparison.

Acknowledgements: The comments of an anonymous referee helped to significantly improve the paper. Funding from the NASA Radiation Science Program, the NASA Earth Observing System/Modeling Analysis and Prediction Program, and the NASA Moderate Resolution Imaging Spectrometer Program is gratefully acknowledged.

References

- Barker, H. W., 1996: A parameterization for computing grid-averaged solar fluxes for inhomogeneous marine boundary layer clouds, part I: methodology and homogeneous biases. *J. Atmos. Sci.*, **53**, 2289-2303.
- Barker H. W., and P. Räisänen, 2004: Neglect by GCMs of subgrid-scale horizontal variations in cloud-droplet effective radius: A diagnostic radiative analysis. *Q. J. R. Meteor. Soc.*, **130**, 1905-1920.
- Cahalan, R. F., W. Ridgway, W. J. Wiscombe, T. L. Bell and J. B. Snider, 1994: The albedo of fractal stratocumulus clouds. *J. Atmos. Sci.*, **51**, 2434-2455.
- Chou, M.-D., M. J. Suarez, C.-H. Ho, M. M.-H. Yan, and K.-T. Lee, 1998: Parameterizations for cloud overlapping and shortwave single-scattering properties for use in general circulation and cloud ensemble models. *J. Climate*, **11**, 202-214.
- Derber, J. C., D. F. Parrish, and S. J. Lord, 1991: The new global operational analysis system at the National Meteorological Center. *Weath. Forec.*, **6**, 538–547.
- Harshvardhan, and D. A. Randall, 1985: comments on “The parameterization of radiation for numerical weather prediction and climate models”. *Mon. Wea. Rev.*, **113**, 1832-1833.
- Hu, Y. X., and K. Stamnes, 1993: An accurate parameterization of the radiative properties of water clouds suitable for use in climate models. *J. Climate*, **6**, 728–742.
- Khairoutdinov, M., D. A. Randall, and C. DeMott. 2005: Simulations of the Atmospheric General Circulation Using a Cloud-Resolving Model as a Superparameterization of Physical Processes. *J. Atmos. Sci.*, **62**, 2136–2154.

- Kiehl, J.T. and K.E. Trenberth, 1997: Earth's annual global mean energy budget. *Bull. Amer. Meteor. Soc.*, **78**, 197–208.
- King, M. D., W. P. Menzel, Y. J. Kaufman, D. Tanré, B.-C. Gao, S. Platnick, S. A. Ackerman, L. A. Remer, R. Pincus, and P. A. Hubanks, 2003: Cloud and aerosol properties, precipitable water, and profiles of temperature and water vapor from MODIS. *IEEE Trans. Geosc. Rem. Sens.*, **41**, 442-458.
- Moody, E. G., M. D. King, S. Platnick, C. B. Schaaf, and F. Gao, 2005: Spatially complete global spectral surface albedos: Value-added datasets derived from Terra MODIS land products. *IEEE Trans. Geosci. Remote Sens.*, **43**, 144-158.
- Oreopoulos, L., and R. Davies, 1998: Plane parallel albedo biases from satellite observations. Part I: Dependence on resolution and other factors. *J. Climate*, **11**, 919-932.
- Oreopoulos, L., M.-D. Chou, M. Khairoutdinov, H. W. Barker, and R. F. Cahalan, 2004: Performance of Goddard Earth Observing System GCM Column Radiation Models under heterogeneous cloud conditions. *Atmos. Res.*, **72**, 365-382.
- Oreopoulos, L., and R. F. Cahalan, 2005: Cloud inhomogeneity from MODIS. *J. Climate*, **18**, 5110–5124.
- Pincus, R., S. A. McFarlane, and S. A. Klein, 1999: Albedo bias and the horizontal variability of clouds in subtropical marine boundary layers: observations from ships and satellites. *J. Geophys. Res.*, **104**, 6183-6191.
- Räisänen, P., G. A. Isaac, H. W. Barker, and I. Gultepe, 2003: Solar radiative transfer for stratiform clouds with horizontal variations in liquid-water path and droplet effective radius. *Q. J. R. Meteor. Soc.*, **129**, 2135-2149.

- Räisänen, P., H. W. Barker, M. F. Khairoutdinov, J. Li, and D. A. Randall, 2004: Stochastic generation of subgrid-scale cloudy columns for large-scale models. *Quart. J. Roy. Meteor. Soc.*, **130**, 2047–2067.
- Rossow, W. B., C. Delo, and B. Cairns, 2002: Implications of the observed mesoscale variations of clouds for the Earth’s radiation budget. *J. Climate*, **15**, 557-585.
- Scheirer, R. and A. Macke, 2003: Cloud inhomogeneity and broadband solar fluxes. *J. Geophys. Res.*, 108(D19), 4599, doi:10.1029/2002JD003321.
- Stephens, G. L., 1988: Radiative transfer through arbitrarily shaped optical media. Part I: A general method of solution. *J. Atmos. Sci.*, **45**, 1818-1836.

Figure Captions

Figure 1. Global monthly-averaged PPH albedo and B_1^R and B_2^R biases of liquid clouds from MODIS Terra and MODIS Aqua Level-3 data for July 2003 and January 2004 (full-column calculations for the part of the gridboxes covered by liquid clouds).

Figure 2. Normalized frequency of occurrence distributions of monthly-averaged B_1^R biases from MODIS Terra and MODIS Aqua full-column calculations.

Figure 3. Monthly-averaged Terra MODIS B_1^R bias from full-column calculations. Top panel is for July 2003 and bottom panel is for January 2004.

Figure 4. Monthly-averaged full-column (FC) and cloud-only (CO) B_1^R biases for Northern Hemisphere land and ocean gridboxes from combining MODIS Terra and MODIS Aqua Level-3 data for July 2003 and January 2004 (for the portion of gridboxes covered by liquid clouds).

Figure 5. Combined Terra-Aqua global average *SWCRF* bias (absolute value) due to optical thickness only horizontal variability from five different types of full-column calculations (see text for details).

Figure 6. Relationship between monthly-averaged χ and B_1^R from all MODIS Terra July 2003 $1^\circ \times 1^\circ$ gridboxes with liquid clouds. Atmospheric and surface effects are included (full-column calculations).

Figure 7. Top panel: Zonal variation of monthly-averaged χ for liquid clouds from combining Terra and Aqua data for July 2003 and January 2004. Bottom panel: Zonal variation of combined absolute TOA *SWCRF* monthly biases from type (5) full-column calculations.

Figure 8. Broadband albedo at SZA=60° vs. r_e for clouds with visible (band 1 of our RT model) optical thickness 15 (solid line) and LWP=96 gm⁻² (dashed line). In the latter case, cloud optical thickness varies with r_e because of changes in cloud extinction. No atmospheric effects were accounted for and the surface is black.

Figure 9. Normalized frequency of occurrence distributions of monthly-averaged B_1^R and B_2^R biases from MODIS Terra for July 2003. Atmospheric and surface effects are included (full-column calculations).

Figure 10. Top panel: Monthly-averaged atmospheric absorptance bias (B_1^A) versus monthly-averaged albedo bias (B_1^R) for Terra July 2003 for isolated clouds (cloud-only calculations, i.e., the atmospheric absorptance bias is equal to the cloud absorptance bias). Bottom panel: As in top panel, but with atmospheric and surface albedo effects included (full-column calculations, i.e., the atmospheric absorptance bias corresponds to the entire atmospheric column).

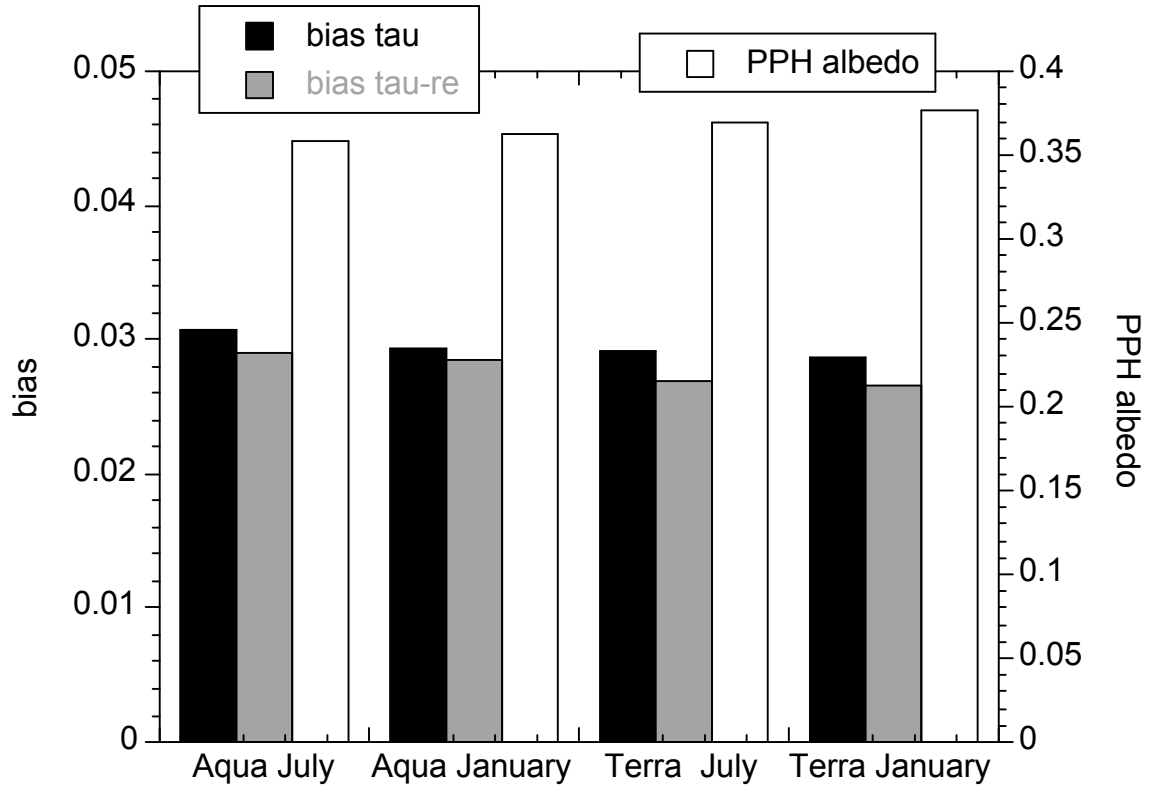


Figure 1. Global monthly-averaged PPH albedo and B_1^R and B_2^R biases of liquid clouds from MODIS Terra and MODIS Aqua Level-3 data for July 2003 and January 2004 (full-column calculations for the part of the gridboxes covered by liquid clouds).

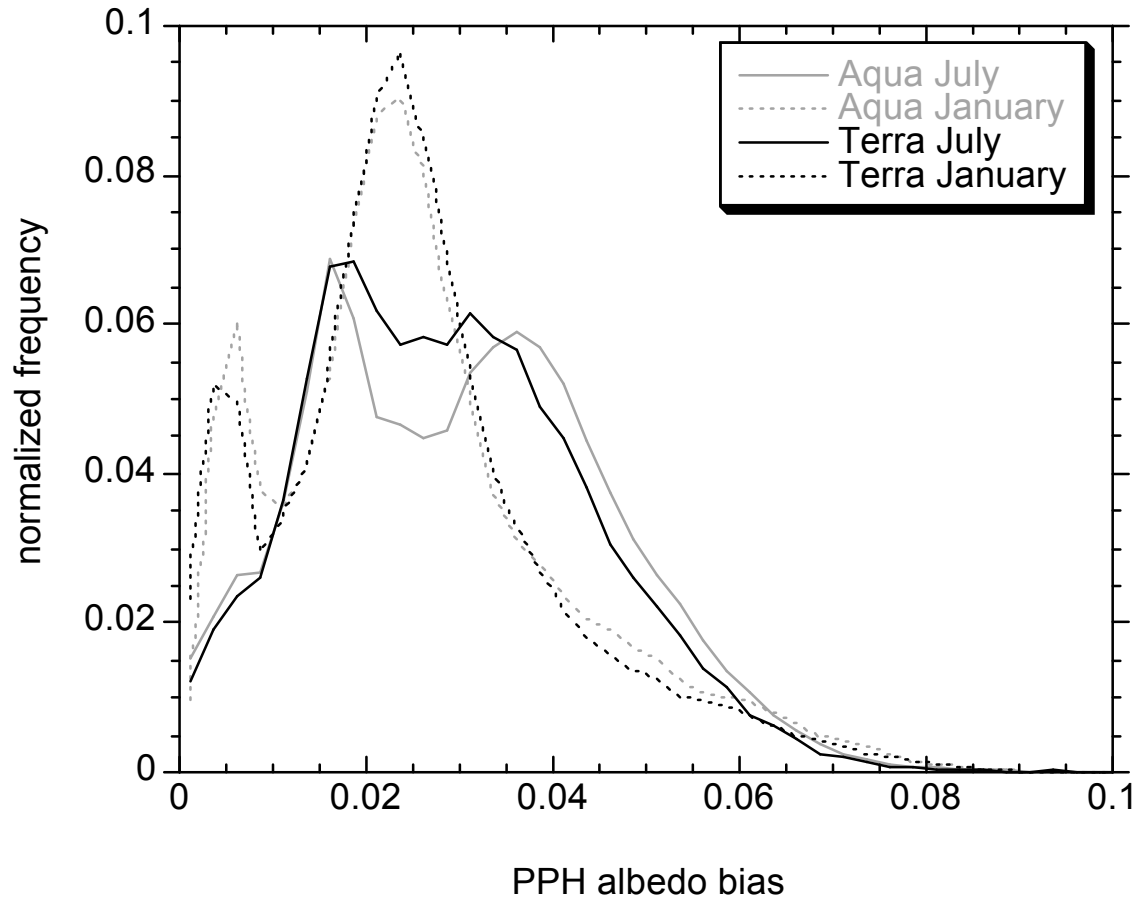


Figure 2. Normalized frequency of occurrence distributions of monthly-averaged B_1^R biases from MODIS Terra and MODIS Aqua full-column calculations.

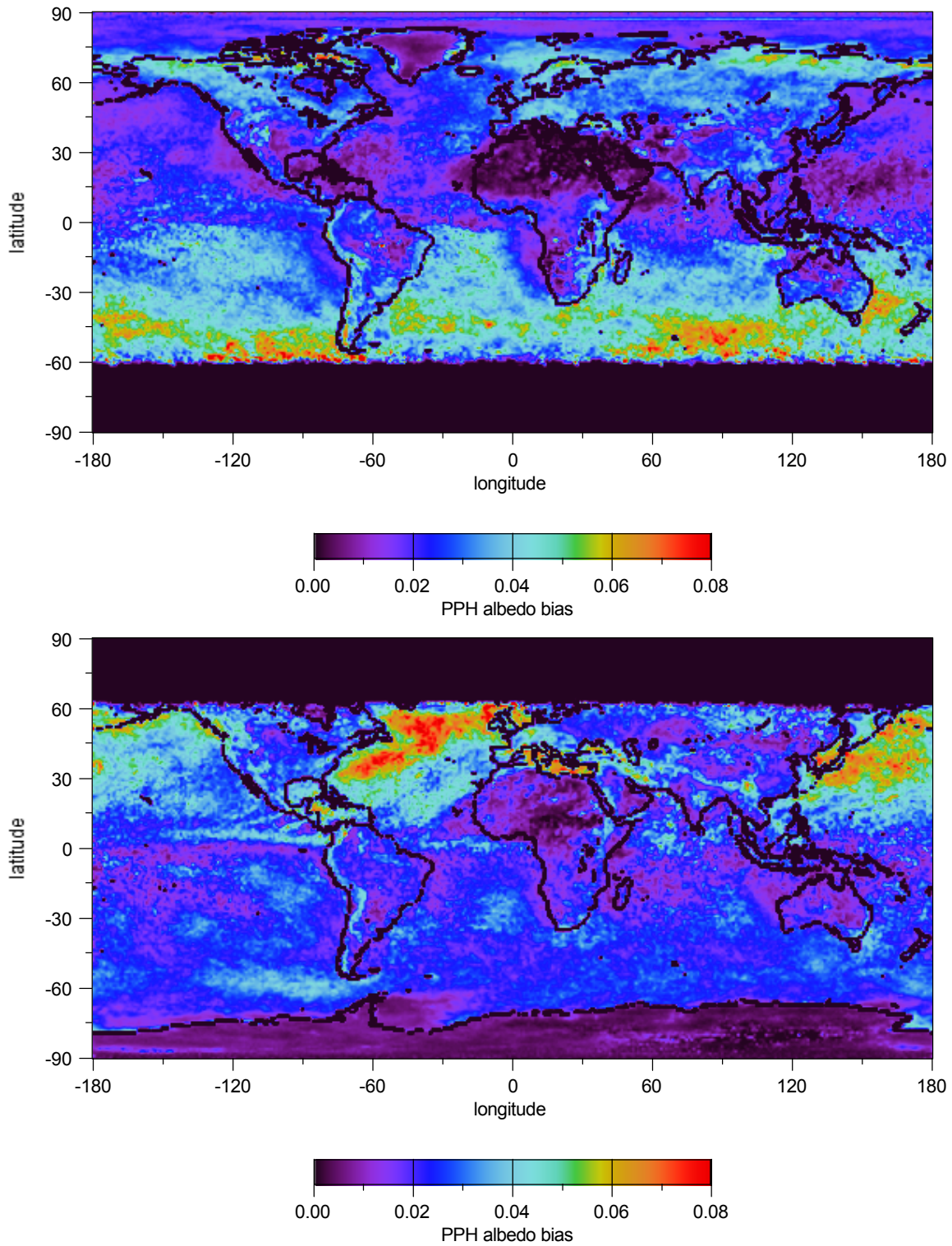


Figure 3. Monthly-averaged Terra MODIS B_1^R bias from full-column calculations. Top panel is for July 2003 and bottom panel is for January 2004.

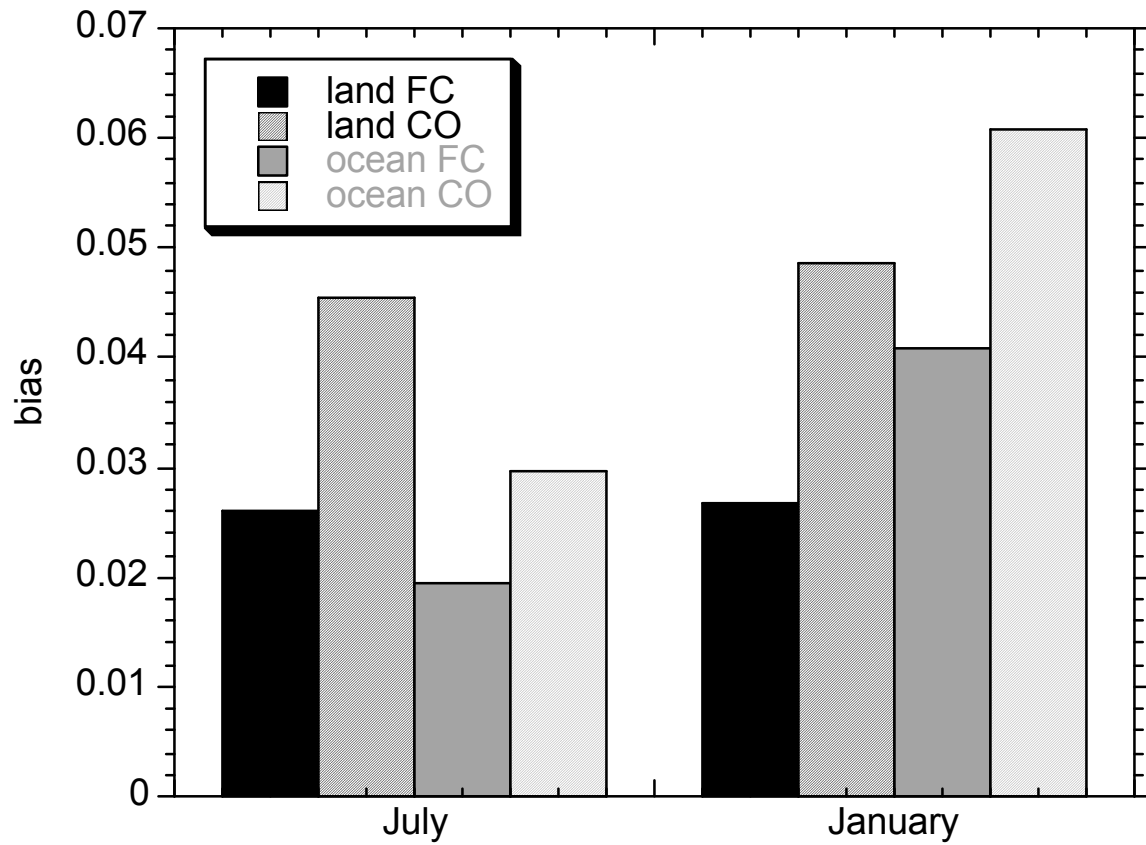


Figure 4. Monthly-averaged full-column (FC) and cloud-only (CO) B_1^R biases for Northern Hemisphere land and ocean gridboxes from combining MODIS Terra and MODIS Aqua Level-3 data for July 2003 and January 2004 (for the portion of gridboxes covered by liquid clouds).

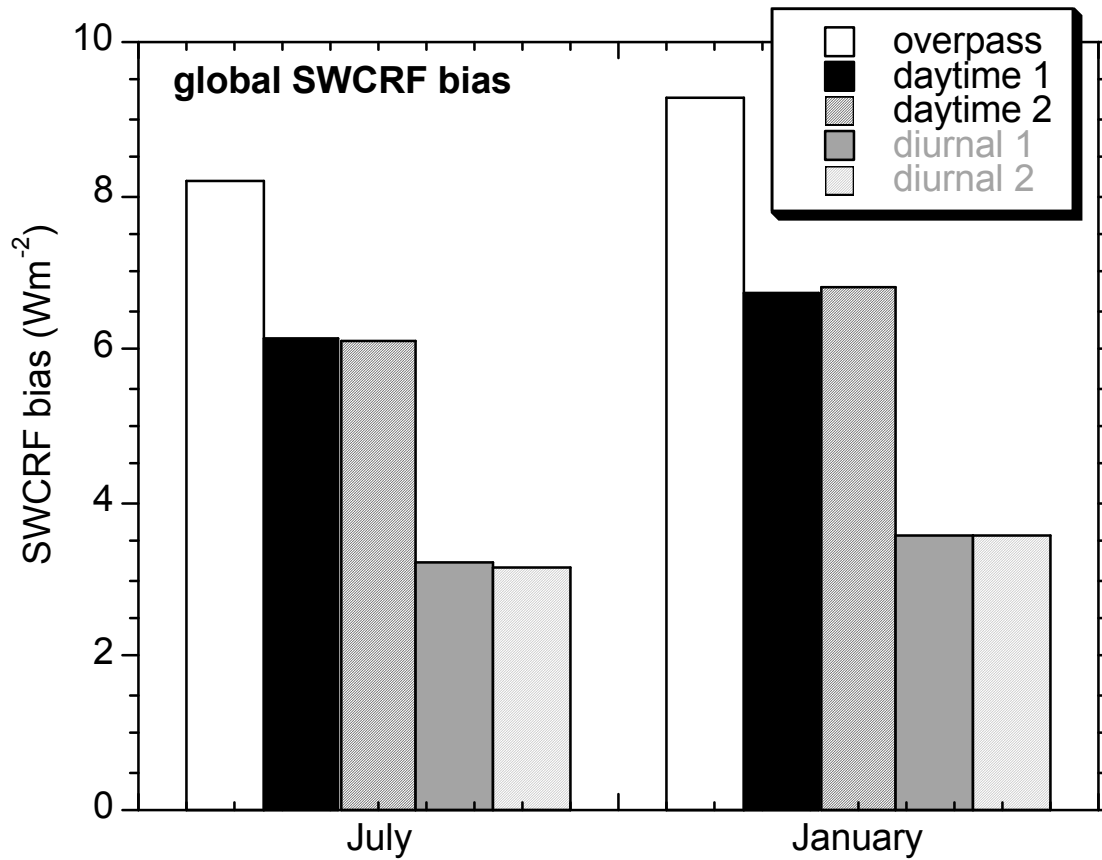


Figure 5. Combined Terra-Aqua global average *SWCRF* bias (absolute value) due to optical thickness only horizontal variability from five different types of full-column calculations (see text for details).

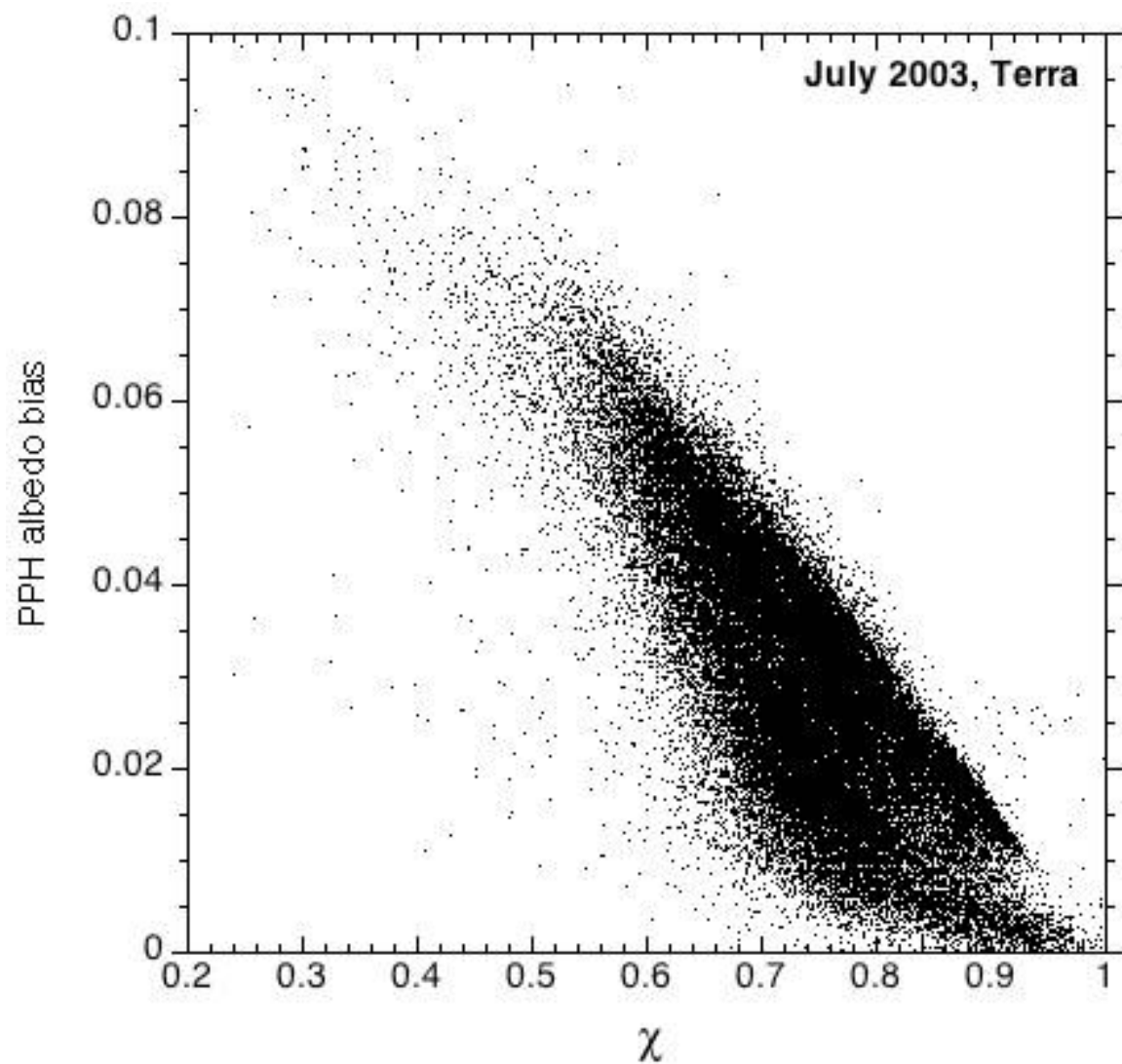


Figure 6. Relationship between monthly-averaged χ and B_1^R from all MODIS Terra July 2003 $1^\circ \times 1^\circ$ gridboxes with liquid clouds. Atmospheric and surface effects are included (full-column calculations).

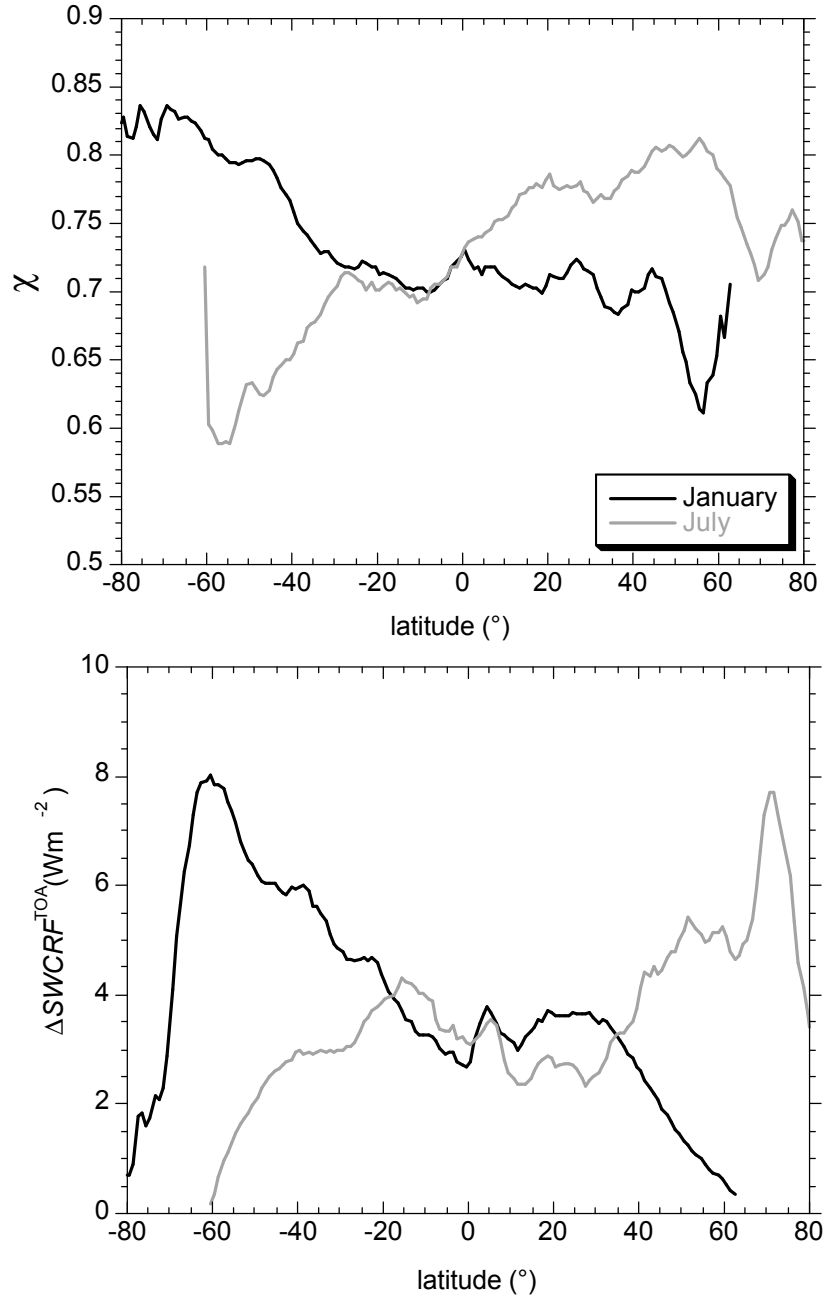


Figure 7. Top panel: Zonal variation of monthly-averaged χ for liquid clouds from combining Terra and Aqua data for July 2003 and January 2004. Bottom panel: Zonal variation of combined absolute TOA *SWCRF* monthly biases from type (5) full-column calculations.

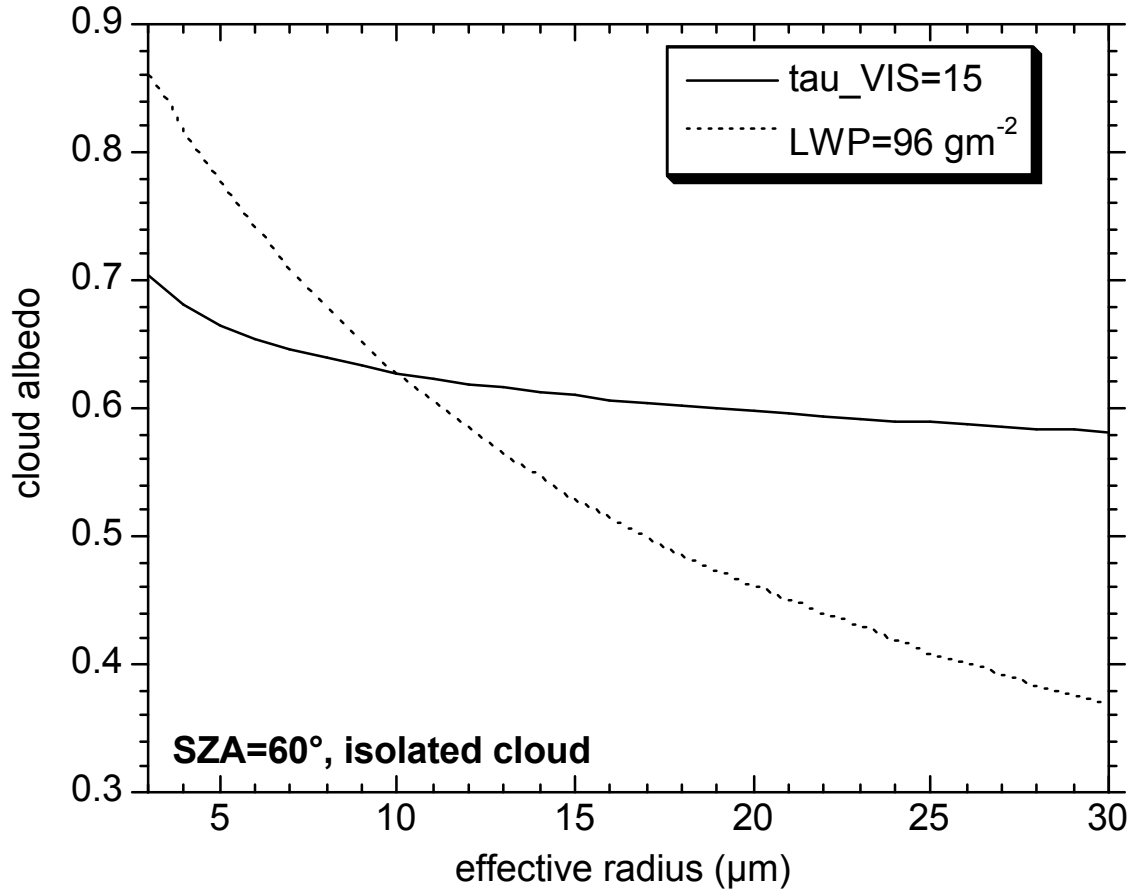


Figure 8. Broadband albedo at SZA=60° vs. r_e for clouds with visible (band 1 of our RT model) optical thickness 15 (solid line) and LWP=96 gm⁻² (dashed line). In the latter case, cloud optical thickness varies with r_e because of changes in cloud extinction. No atmospheric effects were accounted for and the surface is black.

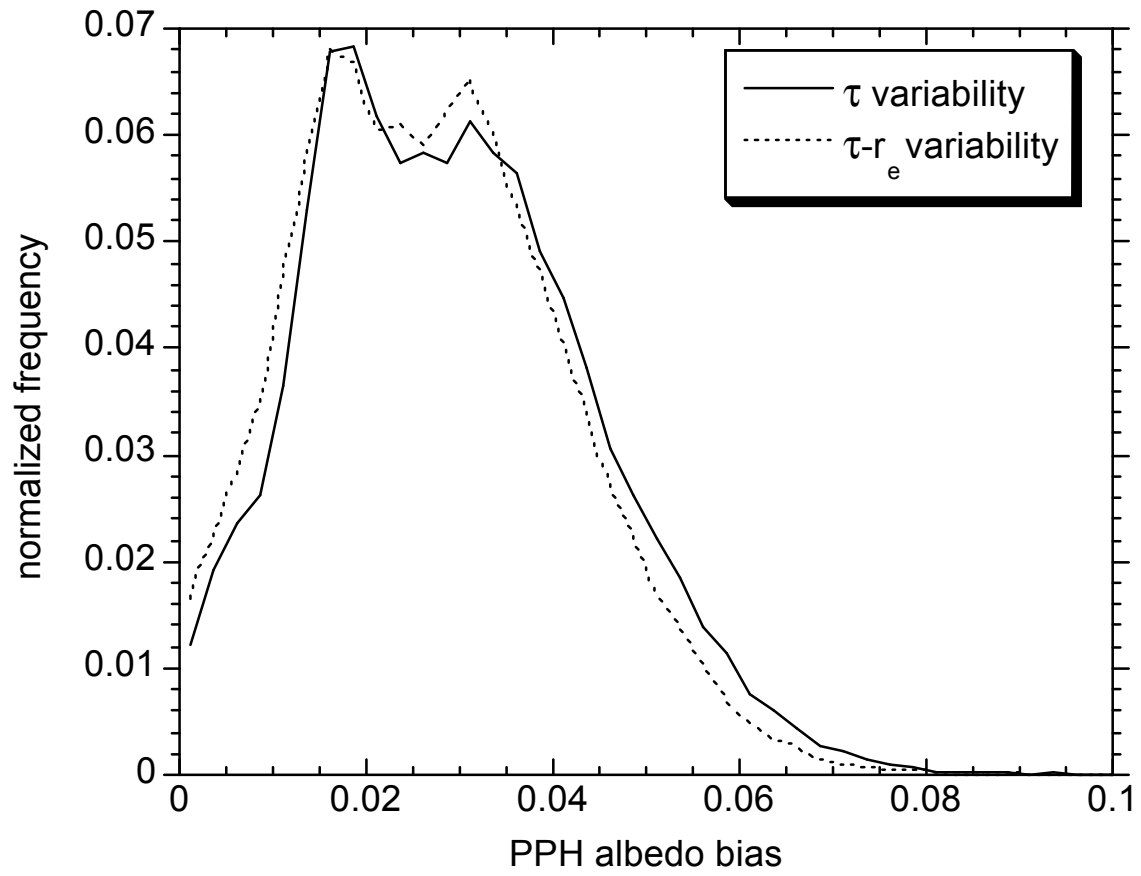


Figure 9. Normalized frequency of occurrence distributions of monthly-averaged B_1^R and B_2^R biases from MODIS Terra for July 2003. Atmospheric and surface effects are included (full-column calculations).

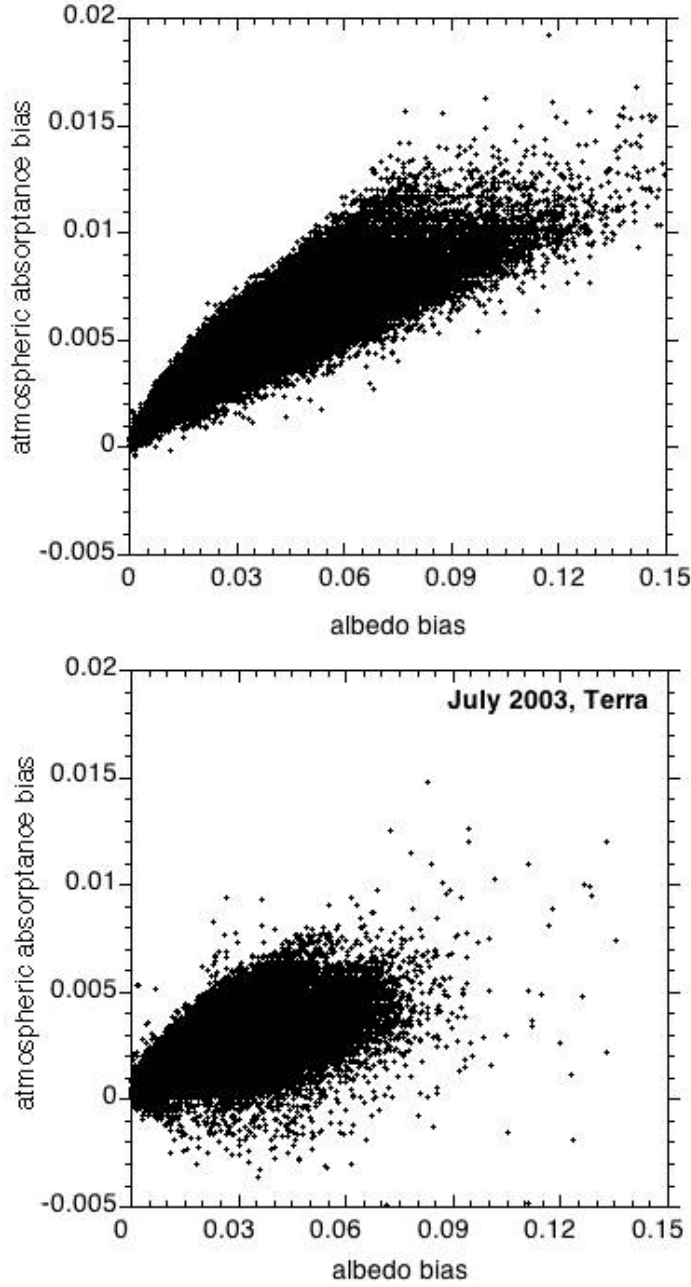


Figure 10. Top panel: Monthly-averaged atmospheric absorptance bias (B_1^A) versus monthly-averaged albedo bias (B_1^R) for Terra July 2003 for isolated clouds (cloud-only calculations, i.e., the atmospheric absorptance bias is equal to the cloud absorptance bias). Bottom panel: As in top panel, but with atmospheric and surface albedo effects included (full-column calculations, i.e., the atmospheric absorptance bias corresponds to the entire atmospheric column).